Theoretical study of single transition metal atom catalysts supported on two-dimensional Nb_2NO_2 for efficient electrochemical CO_2 reduction to CH_4

Song Lu [a], Yang Zhang [a], Fengliu Lou [b,*], Zhixin Yu [a,*]

[a] *Department of Energy and Petroleum Engineering, University of Stavanger, 4036 Stavanger, Norway*
[b] *Beyonder AS, Kanalsletta 2, 4033 Stavanger, Norway*

A B S T R A C T

The design of highly efficient catalysts for electrochemical reduction CO_2 (ECR) to value-add chemicals and fuels is important for CO_2 conversion technologies. In this work, earth abundant transition metal (TM = V, Cr, Mn, Fe, Co and Ni) atoms embedded into two-dimensional (2D) Nb_2NO_2 (TM@Nb_2NO_2) as single-atom catalysts (SACs) for ECR was investigated by first-principles study. We demonstrated that Nb_2NO_2 can be an excellent substrate for anchoring single TM atom due to its excellent stability and electronic conductivity. Besides, V, Cr and Ni@Nb_2NO_2 could effectively promote CO_2 adsorption and reduction. All TM@Nb_2NO_2 exhibit high selectivity towards CH_4, and V, Cr and Ni@Nb_2NO_2 show low limiting potentials. The activity origin was revealed by analysing adsorption energy, d band centre, bonding/antibonding population and the change of valence state of TM atoms.

1. Introduction

With the rapid development of the global economy, energy crisis and environment issues have become increasingly prominent. Carbon dioxide (CO_2) is a primary greenhouse gas, while it could also be a valuable carbon source. In recent years, electrochemical CO_2 reduction reaction (ECR) has received considerable attention among various CO_2 conversion technologies due to numerous advantages [1,2]. For instance, ECR can be driven under ambient temperature and pressure using renewable energy source such as wind and solar power [3,4]. The external voltages as well as electrolytes solutions can be adjusted for the generation of specific products. Furthermore, ECR technology could not only mitigate CO2 emission, but also effectively convert CO_2 to value-added chemicals and fuels, which has been regarded as an appealing technology path for closing the carbon circle [5–7]. Nevertheless, physicochemical properties of the CO_2 molecule make electrochemical conversion of CO_2 challenging [8,9]. In the past decades, metals or related oxides, carbon-based materials and nanocomposites have been widely investigated as electrocatalysts for ECR. Despite that great progress has been made to exploit electrocatalysts for ECR, the process is still impeded by the sluggish kinetics, poor product selectivity, catalyst stability, and high overpotential [10–13]. Taking copper as an example, it can

electrochemically convert CO_2 to CH_4 with a high overpotential around 0.9 V, but the selectivity to specific products is low [14,15]. Therefore, it is highly desirable to develop electrocatalysts with high activity and selectivity for ECR.

It has been well established that the catalytic activity can be improved by reducing the size of catalysts. Specifically, single atoms catalysts (SACs) with single atom as active centre have aroused huge interest due to maximum atom utilization and excellent performance in various catalytic reactions such as water splitting, CO_2 reduction, N_2 reduction, etc. [16–20]. It is worth noting that the preparation of SACs is a challenge because single atoms with high surface energy are easy to aggregate into clusters, leading to catalyst deactivation. Thus, a suitable support which could offer anchoring sites and possesses good stability will greatly improve the activity of SACs. Two-dimensional (2D) materials are appealing substrates for anchoring single transition metal atom due to their unique structures and electronic properties [21–23]. Moreover, it has been disclosed that the interaction between p-orbital of substrates and d-orbitals of single transition metal atom are beneficial for highly effective electrocatalysts [24,25]. For example, single transition metal atoms embedded into graphene, graphitic carbon nitride (g-C_3N_4), graphyne, boron nitride (BN), phthalocyanine (PC), etc. have been widely studied as promising SACs for CO_2 reduction [26–29].

Recently, a family of 2D transition metal carbides, nitrides and carbonitrides, known as MXenes, were reported and synthesized from the layered $M_{n+1}AX_n$ phase [30]. In $M_{n+1}AX_n$, M stands for early transition metals, A denotes the group 13 or 14 elements, X denotes C or N, and n is between 1 and 3 [31]. There are a variety of MXenes that have been predicted and synthesized experimentally, which are explored for applications in many fields [32]. For instance, Li et al. reported that MXenes from the group IV to VI series are active for CO_2 capture, while Cr_3C_2 and Mo_3C_2 are promising catalysts for CO_2 conversion to CH_4 [33]. Both simulation study and experimental work have shown that MXenes have large surface areas, excellent electronic conductivity, tunable surface composition and great stability [32,34]. Thanks to these merits, MXenes have also been demonstrated to be promising substrates for anchoring single transition metal atoms in catalytic reactions [35]. Generally, $M_{n+1}N_n$ is more difficult to synthesize compared to $M_{n+1}C_n$. Interestingly, it has been demonstrated that nitride MXenes exhibit better conductivity in comparison with carbide MXenes [36]. During synthesis, the basal plane of MXenes could be functionalized by various atoms or groups including O, OH and F, which affect their inherent properties [30]. Recent investigations have demonstrated that under high temperature treatment the F group can be eliminated and OH group can be converted to O groups [37,38]. Studies have confirmed that these different functional groups could tune the work function and electronic properties of MXenes [39].

Nb-based MXenes have gained great attention in energy storage and conversion [40,41]. Pt-doped Nb-based MXene has been reported to be an excellent bifunctional OER/ORR catalyst [42], while nitride Nb_2N for ECR has not been studied. In this work, for the first time, we investigated the single transition metal atoms (V, Cr, Mn, Fe, Co, Ni) embedded O group terminated Nb_2N monolayer (Nb_2NO_2) as ECR catalysts by first-principles calculation. It is found that Nb_2NO_2 can be an ideal support for anchoring sing TM atoms because of excellent stability and conductivity. TM@Nb_2NO_2 show excellent CO_2 adsorption capacity, which benefits CO_2 activation and reduction. Among six SACs catalysts, V, Cr and Ni@ Nb_2NO_2 are identified as efficient electrocatalysts for ECR to CH_4, with smaller limiting potential of − 0.45, − 0.47 and − 0.28 V, respectively. Meanwhile, the origin of the ECR activity was revealed by several key descriptors.

2. Computational method

All calculations were carried out by spin-polarized density functional theory (DFT) in the Vienna Ab initio Simulation Package (VASP) with projector augmented wave (PAW) [43,44]. The generalized gradient approximation (GGA) implemented Perdew-Burke-Ernzerhof (PBE) was used to calculate the exchange-correlation energy [45,46]. The empirical correction (DFT-D3) was employed to describe the van der Waals (vdW) interactions [47]. The parameter for dipole correction along z-direction are considered in our calculations. DFT+U calculations are also considered for single TM atoms. The values of U−J were set to be 2.72, 2.79, 3.06, 3.29, 3.42 and 3.4 eV for V, Cr, Mn, Fe, Co, and Ni, respectively [18]. A $3 \times 3 \times 1$ TM@Nb_2NO_2 containing 45 atoms was constructed by anchoring one TM atom in site1 (N site) and site 2 (Nb site) (Fig. 1a). The 18 Å thickness vacuum region in the z-direction was added to eliminate the spurious interactions from periodic boundary. The cutoff energy was set to 500 eV. The K-points for geometry optimization and electronic calculations were set to be $6 \times 6 \times 1$ and $10 \times 10 \times 1$, respectively. The convergence of energy and force was set to be 1.0×10^{-5} eV and 1.0×10^{-2} eV/Å, respectively. Solvent effect was included in our calculations by using implicit solvent model based on VASPsol, and the dielectric constant of water was 78.4 [48]. Moreover, to explore structure stability, the ab initio molecular dynamics (AIMD) simulation was performed in NVT ensemble and phonon spectra was calculated based on the density functional perturbation theory (DFPT)
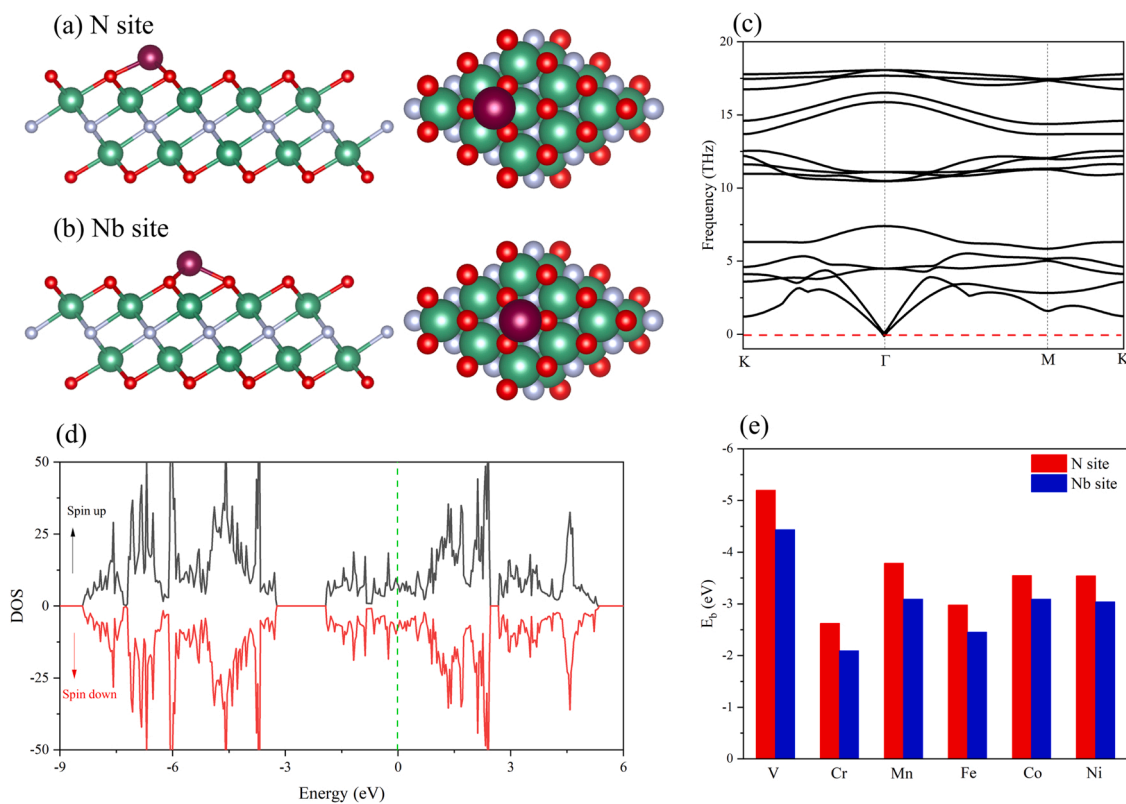

Fig. 1. The two possible adsorption sites for TM atoms (a)N site and (b) Nb site, where the whitesmoke, red, turquoise and purple ball denote the N, O, Nb and TM atoms; (c) The phonon curves of Nb_2NO_2; (d) The total density of state of Nb_2NO_2, where the green dash line is Fermi energy level; (e) The binding energies of TM atoms on N site and Nb site.

[49,50]. The TM atom transition energy barrier on Nb_2NO_2 monolayer was calculated by the climbing image nudged elastic band method (CINEB) [51], transition states were confirmed by vibration frequency analysis. The Bader charge analysis was used to analyze electron transfer [52].

The binding energy (E_b) of TM atoms on Nb_2NO_2 monolayer was calculated by Eq. 1:

$$E_b = E(TM@Nb_2NO_2) - E(TM) - E(Nb_2NO_2) \qquad (1)$$

where $E(TM)$, $E(Nb_2NO_2)$ and $E(TM@Nb_2NO_2)$ denote the total energies of single TM atom, Nb_2NO_2, and $TM@Nb_2NO_2$, respectively. With such definition, a more negative value indicates a stronger binding of TM atoms to the Nb_2NO_2 substrate.

The gas adsorption energy (E_{ads}) was calculated by Eq. 2:

$$E_{ads} = E(gas@Nb_2NO_2) - E(gas) - E(Nb_2NO_2) \qquad (2)$$

where $E(gas)$, $E(Nb_2NO_2)$ and $E(gas@Nb_2NO_2)$ are the total energies of gas, Nb_2NO_2 and gas adsorbed Nb_2NO_2.

The Gibbs free energy of ECR were calculated by the computational hydrogen electrode (CHE) method [53]. After intermediate was adsorbed on the surface of catalyst, the translation and rotation freedom could be ignored and only vibration freedom is contributed to the entropy. The free energy of H^+/e^- pair is equivalent to the chemical potential of H_2 at standard conditions. The Gibbs free energy change (ΔG) can be obtained by Eq. 3:

$$\Delta G = \Delta E + \Delta E(ZPE) - T\Delta S + \Delta G(pH) + \Delta G(U) \qquad (3)$$

in which ΔE was the energy difference between reactants and products directly obtained from DFT calculations, $\Delta E(ZPE)$ and ΔS are zero-point energy correction and entropy change at temperature T of 298.15 K. $\Delta G(pH)$ is the free energy correction due to the effect of H concentration, and was calculated by the formula $\Delta G(pH) = k_BTln10 \times pH$. In this work, the pH value was set to be zero under acidic condition. $\Delta G(U)$ is the contribution of the applied electrode potentials. The limiting potential (U_L) from potential-determining step (PDS) can be obtained by Eq. 4:

$$U_L = -\Delta G_{max}/e \qquad (4)$$

where ΔG_{max} is the maximum free energy change in the ECR process along the most favourable pathway.

3. Result and discussion

3.1. Structure and stability of Nb_2NO_2

After geometry optimization, the obtained lattice parameter a of clean Nb_2N monolayer is 3.11 Å, consistent with previous study [54]. Nb_2N monolayer shows a hexagonal symmetry with P63/mmc space group. O was then added on the centre of three Nb atoms, similar to the O functionalized Ti_2C MXene (Fig. 1a and b) [55]. The binding energy (E_b) of O on Nb_2N monolayer was calculated by the equation: $E_b = (E(Nb_2NO_2) - E(O_2) - E(Nb_2N))/2$, where $E(Nb_2NO_2)$, $E(O_2)$, $E(Nb_2N)$ are the total energy of Nb_2NO_2, O_2 and Nb_2N [56]. A negative value of $E_b = -5.34$ eV demonstrates that Nb_2N monolayer can be easily covered by O atoms. It is possible for O group transforming to OH during ECR process. Therefore, we calculated the Gibbs free energy for H adsorption on O atoms, with $\Delta G*H$ of -0.16 eV. A moderate $\Delta G*H$ indicates that the proton can easily adsorb on and desorb from the surficial O atom, which may promote protonation of the ECR intermediates. The phonon curves and AIMD simulation were performed to check its stability, as shown in Fig. 1c and Fig. S1. There are no imaginary bands in phonon spectra. The fluctuation of the total energy of Nb_2NO_2 is quite small and around the equilibrium. Meanwhile, the structure does not show any obvious changes, confirming that Nb_2NO_2 monolayer possesses excellent stability. On the other hand, the calculated density of state of

Nb_2NO_2 exhibits metallic behaviour, indicting good capability for electron transfer (Fig. 1d). This endows Nb_2NO_2 monolayer excellent electrical conductivity, a prerequisite for an ideal substrate for SACs used in ECR.

3.2. Structure and stability of $TM@Nb_2NO_2$

The stability of TM anchored Nb_2NO_2 will be the key for the synthesis and application of MXene based SACs. As presented in Fig. 1a and b, there are two possible anchoring sites for single TM atoms: (1) the centre site between three neighbouring N atoms and the top of Nb atom (Nb site), (2) the centre site between three neighbouring Nb atoms and the top of N atom (N site). After structure relaxation, the anchored TM atoms have slight effects on lattice parameters a. The thermodynamic stabilities of $TM@Nb_2N$ were investigated by calculating E_b (Fig. 1e and Table S1). Notably, a more negative value of E_b on N site indicates that TM atoms prefer to bind on N site. Moreover, the transition energy barriers (E_T) of single TM atoms from N to Nb site were calculated to evaluate its kinetic stability. The E_T were calculated by $E_T = E_{TS} - E_{IS}$, in which E_{TS} is the total energy of transition state (TS) from N to Nb site, while E_{IS} is the total energy of TM embedded in N site. As shown in Table S1, the E_T of TM atoms are quite large in the range of 0.87–2.58 eV, implying that it is difficult for TM atoms to diffuse and aggregate into clusters. These results suggest that single TM atom can firmly anchor on N site. We therefore will only consider this site as active site for further study. In addition, Bader charge analysis show that the charge transfer from TM atoms to substrate decreases with the atomic number. Consequently, V and Cr atom present higher oxidation state (+1.08 and +1.02), while Ni atom shows lower oxidation value (+0.50).

3.3. CO_2 adsorption and activation on $TM@Nb_2NO_2$

CO_2 adsorption on the surface of electrocatalysts is important for CO_2 activation and transformation into intermediates such as *COOH and *OCHO [57]. The optimized CO_2 adsorption configurations on $TM@Nb_2NO_2$ were shown in Fig. 2. Obviously, the carbon or oxygen atom of CO_2 molecule is absorbed on TM atoms. Meanwhile, it can be observed that CO_2 molecule is not absorbed on $TM@Nb_2NO_2$ in linear state, but with a certain degree of bending. The corresponding adsorption energies, bond lengths of C—TM and O—TM, bond angles of CO_2 molecule, and charge transfer between TM and CO_2 molecule are summarized in Table 1. It is clear that the bond angle of CO_2 molecule on $TM@Nb_2NO_2$ increases with the atomic number, ranging from 138.39° to 154.34°. Specially, $V@Nb_2NO_2$ greatly deviated from the linear state, which indicates higher CO_2 adsorption capacity. The bond lengths of C—TM and O—TM are quite close to 2.00 Å, demonstrating strong adsorption between substrate and CO_2 molecule, consistent with previous studies [26,58]. The CO_2 adsorption energies on $TM@Nb_2NO_2$ range from -0.77 and -0.30 eV. The negative values indicate that CO_2 adsorption on the SACs is thermodynamically favourable. V, Cr and $Ni@Nb_2NO_2$ exhibit relatively strong interaction with CO_2. Bader charge analysis confirm that there is a significant net charge transfer from V, Cr and Ni atoms to CO_2, with a value of -0.60e, -0.53e, -0.31e, respectively. Thus, CO_2 molecules can be effectively activated by V, Cr and $Ni@Nb_2NO_2$, and these three SACs potentially exhibit high performance for producing specific ECR products.

3.4. Competition between HER and ECR during first protonation

The ECR process starts with the hydrogenation of CO_2 molecule to form *COOH ($* + CO_2 + (H^+ + e^-) \rightarrow$ *COOH) or *OCHO ($* + CO_2 + (H^+ + e^-) \rightarrow$ *OCHO) on active centres by H atom binding O or C atom. However, the side-reaction HER ($* + H^+ + e^- \rightarrow$ *H) may occur due to the direct interaction between proton and TM atoms, resulting in low ECR selectivity. It has been widely accepted that the Gibbs free energy change (ΔG) for *COOH/*OCHO and *H formation can be used to
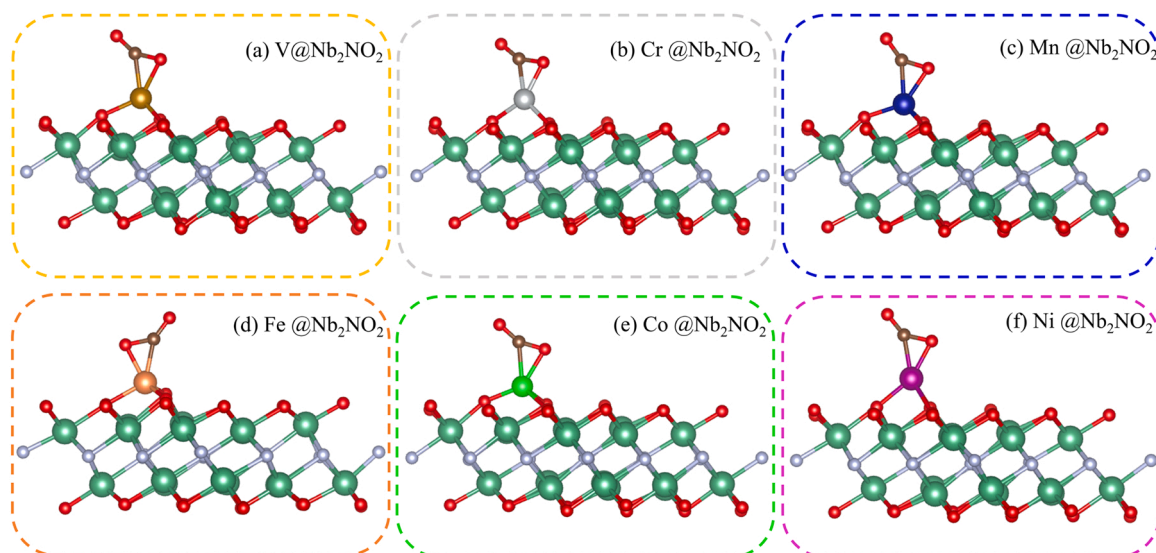
Fig. 2. The most stable CO_2 adsorption configurations on (a) V@Nb_2NO_2, (b) Cr@Nb_2NO_2, (c) Mn@Nb_2NO_2, (d) Fe Ni@Nb_2NO_2, (e) Co@Nb_2NO_2 and (f) Ni@Nb_2NO_2.

Table 1

CO_2 adsorption on TM@Nb_2NO_2: adsorption energy (E_{ads}) with unit eV, the angel of O−C−O with unit °, the bond length of TM−O and TM−C with unit Å, net charge accepted by CO_2 molecule with unit e.

Catalysts	E_{ads} (CO_2)	O−C−O angle	d_{TM-C}	d_{TM-O}	Q
V@Nb_2NO_2	− 0.77	138.39	2.00	1.93	− 0.60
Cr@Nb_2NO_2	− 0.51	142.59	2.00	1.97	− 0.53
Mn@Nb_2NO_2	− 0.34	141.62	2.00	1.93	− 0.58
Fe@Nb_2NO_2	− 0.46	150.77	2.04	2.00	− 0.25
Co@Nb_2NO_2	− 0.30	154.34	2.05	1.99	− 0.26
Ni@Nb_2NO_2	− 0.54	151.74	1.96	1.92	− 0.31

evaluate the ECR selectivity versus HER selectivity [59]. Therefore, $\Delta G_{*COOH/*OCHO}$ were calculated and compared with ΔG_{*H}. As plotted in Fig. 3, all TM@Nb_2NO_2 electrocatalysts prefer ECR (below the diagonal) to HER (above the diagonal). Notably, V, Cr and Fe@Nb_2NO_2 are ECR selective with two favourable initial protonation processes (*COOH and *OCHO), while Ni, Co and Mn@Nb_2NO_2 exhibit ECR selectivity only with one favourable initial protonation step (*COOH or *OCHO). Meanwhile, ΔG_{*OCHO} is smaller than ΔG_{*COOH} for V, Cr and
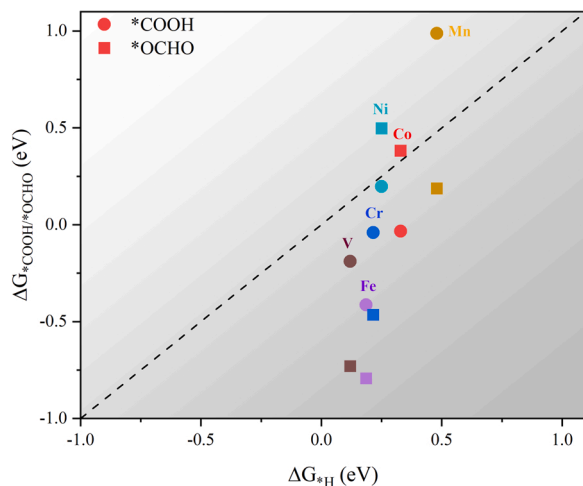

Fig. 3. The Gibbs free energy changes (ΔG (eV)) for the first protonation step in ECR and HER on TM@Nb_2NO_2.

Fe@Nb_2NO_2, demonstrating that the formation of *OCHO is more energetically favourable. Therefore, the *COOH reduction path and the corresponding CO product will not be considered on these three SACs in the further protonation process.

3.5. ECR to C1 products on TM@Nb_2NO_2

The reduction products from CO_2 could involve C_1, C_2 and C_3 due to complex protonation and C−C coupling. However, the formation of high carbon products (C_{2+}) is impossible because C−C coupling will not occur on SACs. Therefore, only C_1 products by accepting 2e to 8e electrons, including CO, HCOOH, HCHO, CH_3OH, CH_4, were investigated in this work. These different products are formed by different number of protons binding C or O atoms. A possible pathway was plotted in Fig. 4 by taking the optimized configuration of intermediates on Fe@Nb_2NO_2 as an example. It is obvious that only TM atom binds with the C or O atoms during the whole ECR process, demonstrating TM atom as active site.

After *COOH or *OCHO formation via accepting first proton-electron pair, further hydrogenation by obtaining a second proton-electron pair will produce *OCHOH or *CO intermediates. Therefore, the binding strength between these two intermediates and active centre will decide HCOOH or CO generation. We calculated the E_{ads} of HCOOH and CO on TM@Nb_2NO_2 (Table 2). For HCOOH formation from *OCHO, V, Cr, Mn and Fe@Nb_2NO_2 show a large E_{ads} with − 1.07, − 1.25, − 0.87 and − 1.51 eV, respectively. For CO formation from *COOH, the E_{ads} of CO on Co and Ni@Nb_2NO_2 are − 1.95 and − 1.73 eV, respectively. It means that both HCOOH and CO could be further protonated on these SACs instead of desorbing from the SACs as final products. In addition, the generation of *OCHOH or *CO on Fe, Co, Cr, Ni and V@Nb_2NO_2 are overall exothermic. The generation of *OCHOH is only slightly endothermic on Mn@Nb_2NO_2, benefiting the further reduction of intermediates.

For further hydrogenation of *OCHOH or *CO, three possible intermediate including *CHO, *COH and *OCH could be generated. Notably, *COH from *CO (*CO + ($H^+ + e^-$) →*COH) on Co and Ni@Nb_2NO_2 underwent a larger energy uphill in comparison with the formation of *CHO (*CO + ($H^+ + e^-$) →*CHO). Similarly, For V, Cr, Mn and Fe@Nb_2NO_2, the formation of *OCH from*OCHOH (*OCHOH + (H^+ + e^-) →*OCH + H_2O) are more energy consuming than the production of *CHO. Thus, it can be concluded that *CHO will be the key intermediates for the third hydrogenation process.
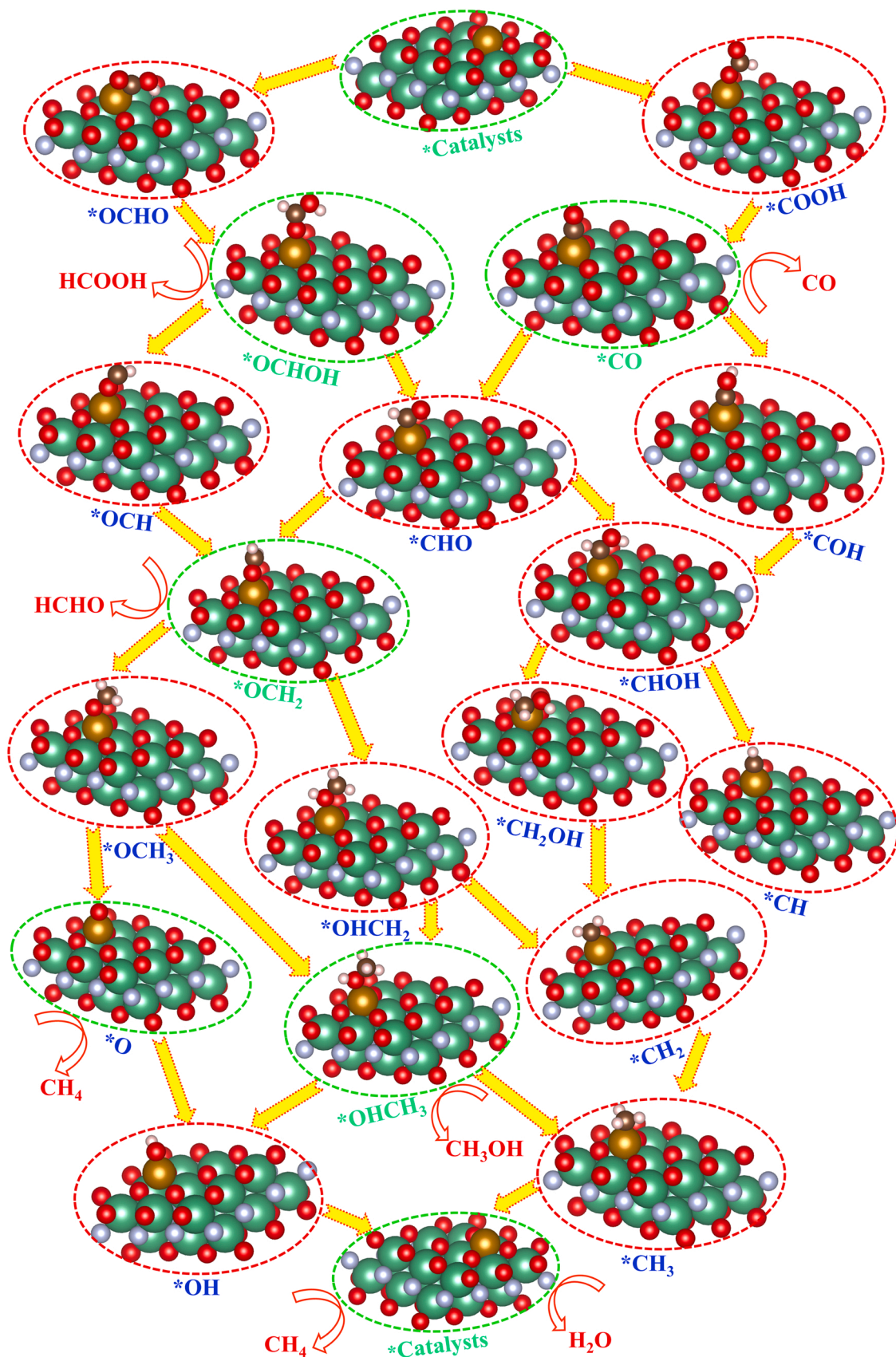
Fig. 4. The optimized configuration of intermediates adsorbed on Fe@Nb$_2$NO$_2$ during the whole ECR process from one-electron to eight-electron products.

Table 2

The adsorption energy of different products CO, HCOOH, HCHO, CH$_3$OH and CH$_4$ with unit eV, and the limiting potential for generating final product CH$_4$ with unit V.
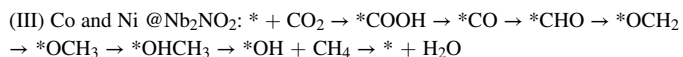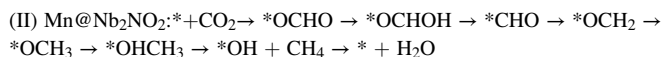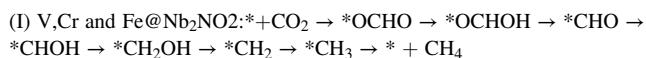
Catalysts	E_{ads} (CO)	E_{ads} (HCOOH)	E_{ads} (HCHO)	E_{ads} (CH$_3$OH)	E_{ads} (CH$_4$)	U_L (CH$_4$)
V@Nb$_2$NO$_2$	–	– 1.07	– 1.59	– 1.15	– 0.35	–0.45
Cr@Nb$_2$NO$_2$	–	– 1.25	– 1.48	– 1.17	– 0.47	–0.47
Mn@Nb$_2$NO$_2$	–	– 1.20	– 0.96	– 0.88	– 0.23	–0.62
Fe@Nb$_2$NO$_2$	–	– 1.51	– 1.06	– 0.75	– 0.41	–0.89
Co@Nb$_2$NO$_2$	– 1.95	–	– 1.08	– 1.07	– 0.38	–0.57
Ni@Nb$_2$NO$_2$	– 1.73	–	– 1.20	– 1.03	– 0.36	–0.28

*OCH$_2$ and *CHOH intermediates can be produced after *CHO accepting the fourth proton-electron pair. It is evident from Fig. 5 that the ΔG of *CHOH on these six SACs show energy uphill, while the ΔG for the formation of *OCH$_2$ on these SACs show energy downhill. Therefore, these TM atoms exhibit strong oxophilicity to form TM−O bonds. The four-electron product HCHO will be desorbed from the electrocatalyst if the interaction between *OCH$_2$ and TM atom is too weak. The calculated E_{ads} of HCHO on these SACs are in the range of − 1.59 to − 0.96 eV, suggesting that it is difficult for HCHO to desorb and thus can be further reduced.

*CHOH then accepted the fifth proton-electron pair to produce *CH and *CH$_2$OH intermediates, while the hydrogenation products of *OCH$_2$ are *OCH$_3$ and *OHCH$_2$. However, ΔG of *CH and *OHCH$_2$ are energetically unfavourable and will not form. In contrast, *CH$_2$OH and *OCH$_3$ will be the key intermediates and participate in later hydrogenation. CH$_3$OH is the six-electron product via *OCH$_3$ + (H$^+$ + e$^-$) →*OHCH$_3$ → * + CH$_3$OH. Nevertheless, the formation of *OHCH$_3$ only show energy downhill on Fe and Mn@Nb$_2$NO$_2$. The E_{ads} on V, Cr, Mn, Fe, Co, Ni@ Nb$_2$NO$_2$ is − 1.15, − 1.17, − 0.88, − 0.75, − 1.07 and − 1.03 eV, respectively. Thus, CH$_3$OH can still be stably bonded with
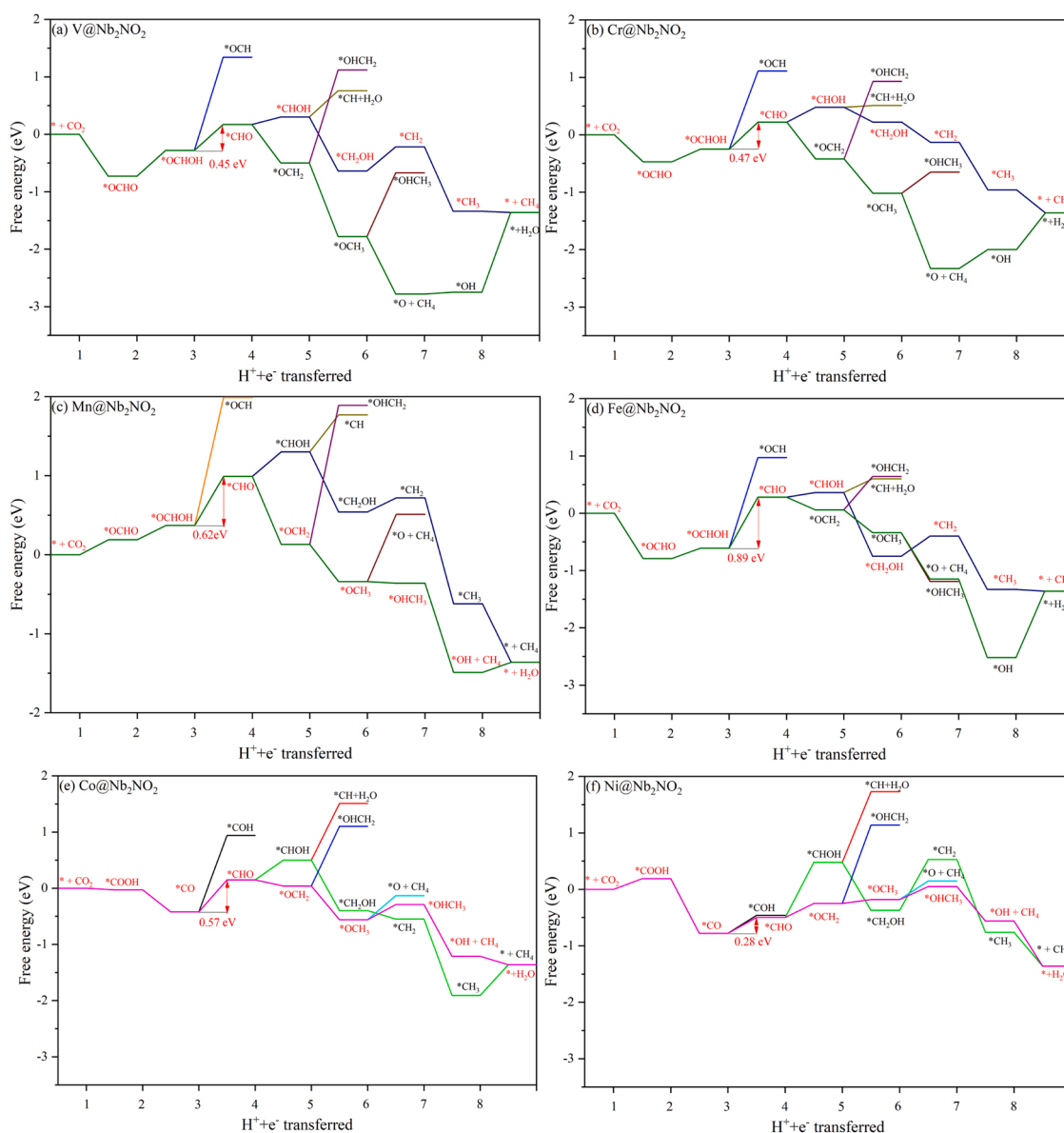
Fig. 5. The Gibbs free energy diagram for ECR on TM@Nb$_2$NO$_2$ to produce the final product CH$_4$ under U = 0 V; the red pathway denotes the optimal pathway.

SACs and further reduced. The eight-electron product CH_4 can be generated from diverse paths such as $*CH_3 + (H^+ + e^-) \rightarrow * + CH_4$, $*OCH_3 + (H^+ + e^-) \rightarrow CH_4 + *O$ and $*OHCH_3 + (H^+ + e^-) \rightarrow CH_4 + *OH$. Remarkably, the E_{ads} of CH_4 on $TM@Nb_2NO_2$ are significantly smaller than the other C_1 products, ranging from -0.47 to -0.23 eV, indicating that CH_4 can easily desorb from the SACs and become the final product. According to principle of minimum free energy increase at each step, the optimized paths for ECR to CH_4 on $TM@Nb_2NO_2$ were concluded as below (Fig. 5):

(I) V,Cr and Fe@Nb2NO2: $*+CO_2 \rightarrow *OCHO \rightarrow *OCHOH \rightarrow *CHO \rightarrow *CHOH \rightarrow *CH_2OH \rightarrow *CH_2 \rightarrow *CH_3 \rightarrow * + CH_4$

(II) Mn@Nb2NO2: $*+CO_2 \rightarrow *OCHO \rightarrow *OCHOH \rightarrow *CHO \rightarrow *OCH_2 \rightarrow *OCH_3 \rightarrow *OHCH_3 \rightarrow *OH + CH_4 \rightarrow * + H_2O$

(III) Co and Ni @Nb2NO2: $* + CO_2 \rightarrow *COOH \rightarrow *CO \rightarrow *CHO \rightarrow *OCH_2 \rightarrow *OCH_3 \rightarrow *OHCH_3 \rightarrow *OH + CH_4 \rightarrow * + H_2O$

Thus, $TM@Nb_2NO_2$ can be promising candidates in electrochemically converting CO_2 to CH_4.

To evaluate the ECR performance of $TM@Nb_2NO_2$, the PDSs and the corresponding U_L were summarized in Table 2. Generally, the lower the value of U_L, the higher the activity of SACs. In path I and II, $*OCHOH \rightarrow *CHO$ was identified as PDS for V, Cr, Mn and Fe@Nb2NO2. The U_L for CH_4 generation on these four SACs are -0.45, -0.47, -0.62 and -0.89 V. The PDS of Co and Ni@Nb2NO2 in path III is $*CO \rightarrow *CHO$, and the corresponding U_L are -0.57 and -0.28 V. Intriguingly, U_L for the ECR to CH_4 on V, Cr, Co and Ni@Nb2NO2 are lower than that the state-of-the-art catalyst Cu (211) (-0.74 V) [60], demonstrating potentially excellent performance of $TM@Nb_2NO_2$ for ECR to CH_4. Particularly, the U_L of Ni@Nb2NO2 is among the best reported in literature. Finally, we investigated the stability of Ni@Nb2NO2 by AIMD simulations with a time step of 3 fs at the temperature of 300 K for 18 ps (Fig. S2). It can be found that Ni atom can still stay at the vacancy, which evidenced that diffusion will not occur.

3.6. Electronic structure of intermediates adsorbed TM@Nb2NO2

The excellent activity of $TM@Nb_2NO_2$ for CH_4 generations is mainly related to the interaction between active TM atom and substrate. As shown in Table S1, the Nb_2NO_2 monolayer is negatively charged by TM atoms. The different amount of charge transfer indicates the different interaction strength. Consequently, the single TM atom with different
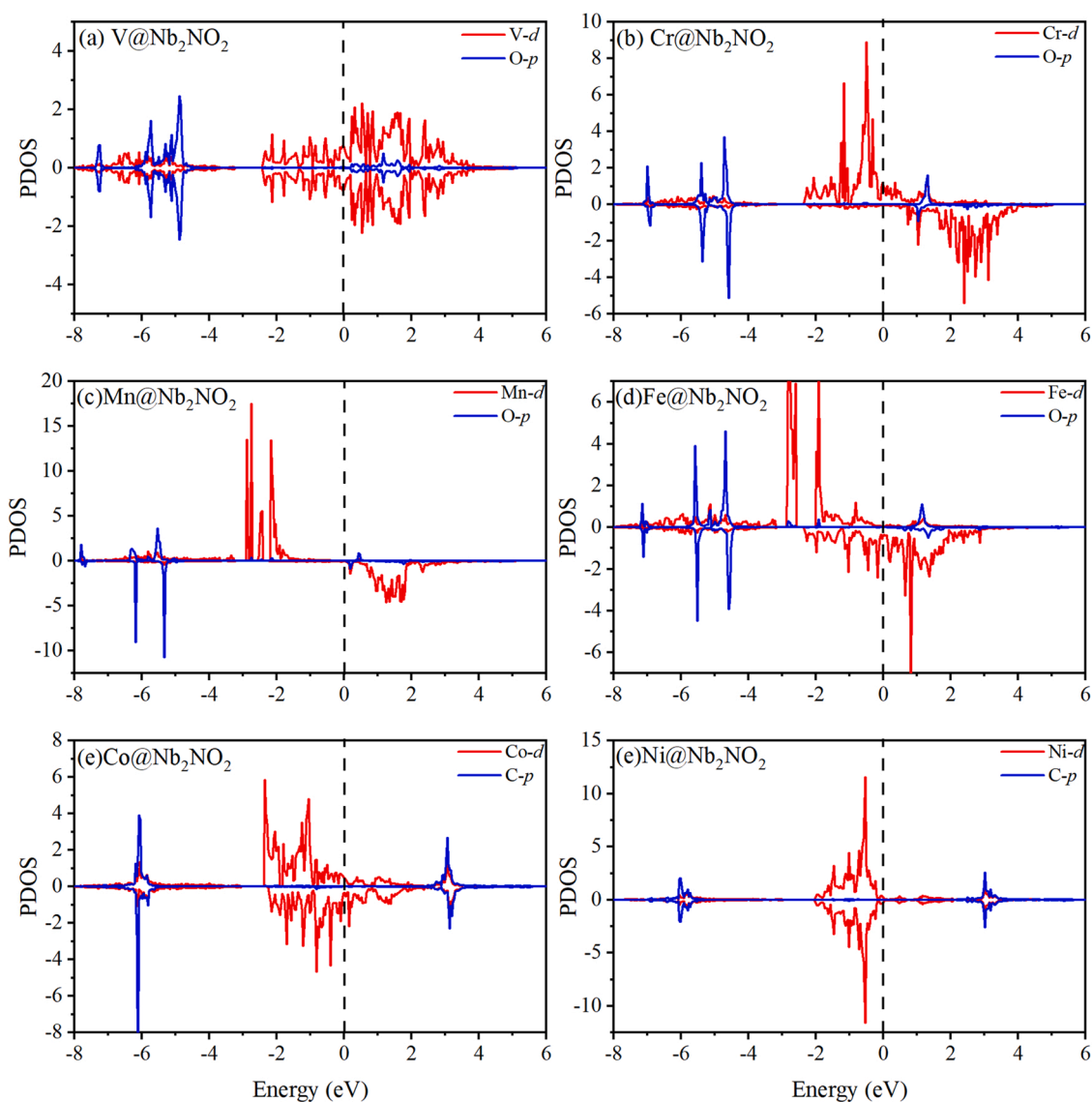

Fig. 6. The PDOS of *OCHOH adsorbed on (a) V, (b) Cr, (c) Mn and (d) Fe@Nb2NO2; and *CO adsorbed on (e) Co@Nb2NO2 and (f) Ni@Nb2NO2; the dashed line represents the Fermi energy level.

positive charge will contribute to different catalytic activity. After intermediate adsorption on the single TM atom, the binding strength between them will directly determine U_L. According to the Sabatier principle, too strong or too weak binding strength will result in low catalytic activity [61]. As shown in Fig. 6, the PDOS of key intermediates from PDSs of TM@Nb$_2$NO$_2$ exhibit deferent interaction between TM and C or O atoms. For instance, the Mn-$3d$ orbitals and the O-$2p$ orbitals of *OCHOH in Mn@Nb$_2$NO$_2$ have slight overlap, contributing to weak binding strength. Fe-$3d$ orbitals interacts greatly with O-$2p$, exhibiting strong interaction. The corresponding adsorption energy of OCHOH on these two SACs is − 0.95 and − 1.51 eV, suggesting that too strong or weak interaction could increase the free energy of PDSs.

3.7. Activity origin of ECR to CH$_4$ on TM@Nb$_2$NO$_2$

We further investigated the activity origin on TM@Nb$_2$NO$_2$ by using descriptors. The PDSs of TM@Nb$_2$NO$_2$ can be assigned to *OCHOH and *CO, therefore we distinguish them by two different areas (palegreen and slateblue in Fig. 7). Since the d-band centre of TM atoms has often been used to correlate the catalytic properties, the locations of d band centres (ε) were calculated and plotted against U_L, as shown in Fig. S3 and Fig. 7a. With the increase of the TM-d electron number, ε shifts to a more negative energy level, resulting in the increase of U_L. When the key intermediate is *OCHOH, there is a good linear relationship between ε and U_L ($U_L = 0.35\varepsilon - 0.40$, $R^2 = 0.97$). For *CO as key intermediate, only Co and Ni@Nb$_2$NO$_2$ are distinguished. Generally, the more negative the value of ε, the weaker the adsorption between intermediates and catalysts. For example, it can be found that Mn@Nb$_2$NO$_2$ shows a lower ε, while the E_{ads} for *OCHOH is smaller, indicating weak adsorption and a large U_L. However, ε is not associated with E_{ads} for a specific TM atom in a small range, because of the neglect of the d-band shape and the effect of the TM-s and p orbitals. Thus, the linear relationship is not apparent (Fig. 7b). For *CO intermediate, the higher ε of Co atoms contributed a strong E_{ads} of *CO and high U_L.

The crystal orbital Hamilton populations (COHP) were employed to analyse the bonding and antibonding states of the TM and key intermediates *OCHOH and *CO [13]. Meanwhile, the integrated COHP (ICOHP) was calculated to give a more quantitative explanation (Fig. S4). For O atom bonding with V, Cr, Mn and Fe@Nb$_2$NO$_2$, it shows obvious antibonding states below Fermi level, demonstrating weak adsorption. The corresponding ICOHP values are − 1.32, − 1.44/− 1.57, − 1.47/− 1.75, − 1.28/− 1.61 eV, respectively. V and Cr@Nb$_2$NO$_2$ have similar antibonding states in spin up state, resulting in similar U_L. For C atom bonding with Co and Ni@Nb$_2$NO$_2$, there is no antibonding state below Fermi level with value of − 2.56/− 2.66 and − 2.40 eV, respectively, indicating strong adsorption. The more negative the ICOHP, the more stable of bonding, thus Fe@Nb$_2$NO$_2$ shows a large U_L. A good linear relationship between ICOHP and U_L was obtained for V, Cr, Mn and Fe@Nb$_2$NO$_2$ ($U_L = 1.58\Phi + 1.70$, $R^2 = 0.86$), disclosing the role of different metal centres in the bonding/antibonding orbital populations.

Recently, charge transfers of active atoms have been reported as descriptor to explain the performance of catalysts [62]. Herein, we calculated the valence state (δ) of TM atoms after adsorbing intermediates. The δ of different atoms for different binding atoms vary in a range from + 0.55 to + 1.32, indicating an increase of charge transfer from TM atoms after intermediates adsorption and different interaction strength between them. Fe atom had the largest $\Delta\delta$ increase of 0.37 after intermediates adsorption, implying a possible strong interaction between Fe and *OCHOH and a large U_L. Meanwhile, an approximate linear relationship ($U_L = -3.02\Delta\delta - 0.31$, $R^2 = 0.86$) was obtained, demonstrating that binding strength between catalysts and intermediates can be represented by $\Delta\delta$. Therefore, ε, Φ and $\Delta\delta$ can be used as descriptors to describe the activity origin well. Meanwhile, the E_{ads} can be a nominal descriptor for the ECR activity to CH$_4$ due to the close connection between energy and electronic structure, while ε, Φ and $\Delta\delta$ can quantitively describe the intrinsic activity of ECR to CH$_4$ on TM@ Nb$_2$NO$_2$. Overall, the results show that Ni@Nb$_2$NO$_2$ is the best
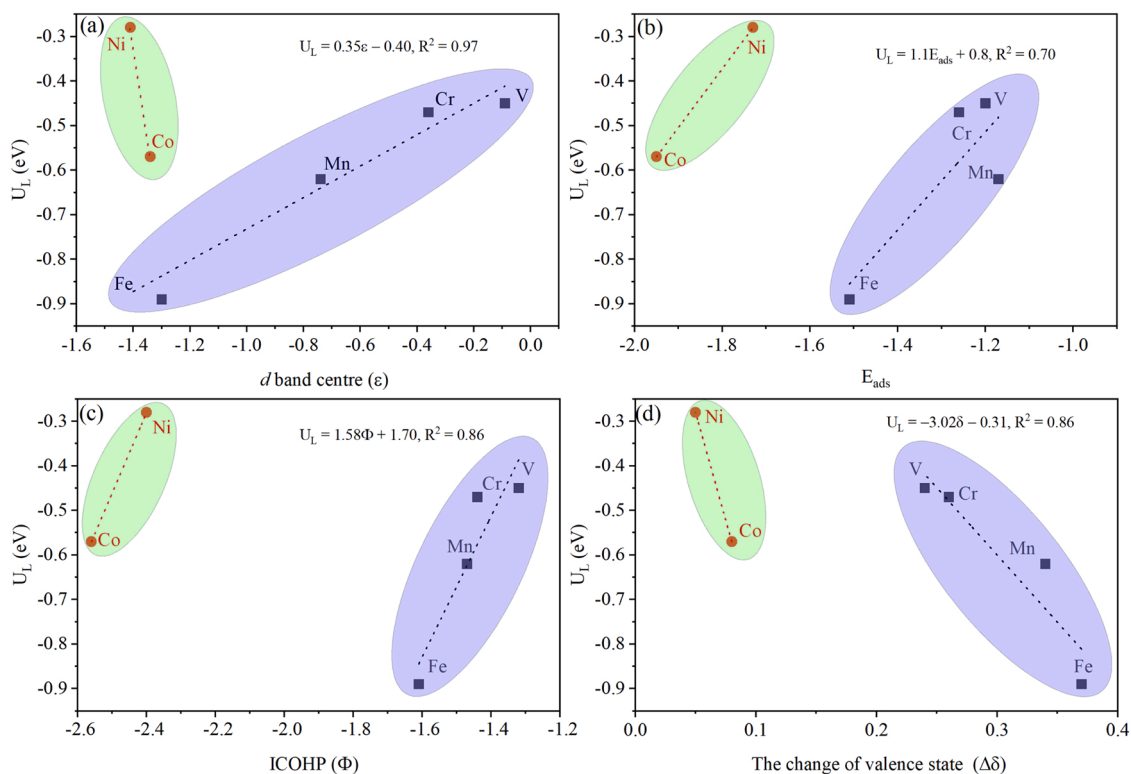

Fig. 7. The limiting potential for the generation of CH$_4$ on TM@Nb$_2$NO$_2$ as a function of (a) d band centre (ε), (b) adsorption energy (E_{ads}), (c) ICOHP (Φ), and (d) the change of TM atom.

ECR catalyst for CH_4 generation, while $Fe@Nb_2NO_2$ is not an ideal catalyst.

4. Conclusion

Single TM atoms (V, Cr, Mn, Fe, Co and Ni) anchored Nb_2NO_2 monolayer as potential SACs for electrochemical CO_2 reduction were studied by first-principles calculation. Results demonstrate that TM atoms can be stably embedded into N site and will not aggregate into clusters. CO_2 molecules can be effectively activated by V, Cr and $Ni@Nb_2NO_2$ due to charge transfer and large adsorption energy. All $TM@Nb_2NO_2$ electrocatalysts exhibit high selectivity for ECR in comparison with HER. The E_{ads} of C_1 products (CO, HCOOH, HCHO, CH_3OH) is too large for them to desorb from the surface of catalysts, while CH_4 can easily desorb due to the small E_{ads}. The PDS on these SACs for ECR to CH_4 can be divided into two categories: *OCHOH to *CHO for V, Cr, Mn and Fe, and *COOH to *CHO for Co and Ni. The U_L for CH_4 generation on V, Cr and $Ni@Nb_2NO_2$ SACs are $- 0.45$, $- 0.47$ and $- 0.28$ V, exhibiting high performance for ECR to CH_4 and is even better than the Cu (211) electrocatalyst. Furthermore, the adsorption energy of the key intermediates (E_{ads}) can serve as a nominal descriptor to indicate ECR activity, while d band center (ε), ICOHP (Φ), the change of valence state ($\Delta\delta$) can quantitatively describe the ECR activity. This work demonstrated that MXene based earth abundant metal SACs are promising for electrocatalytic CO_2 reduction.

CRediT authorship contribution statement

Song Lu: Methodology, Formal analysis, Investigation, Writing – original draft, Writing – review & editing, Visualization. **Yang Zhang:** Investigation, Formal analysis, Writing – review & editing. **Fengliu Lou:** Investigation, Formal analysis, Writing – review & editing. **Zhixin Yu:** Conceptualization, Formal analysis, Validation, Resources, Supervision, Writing – review & editing

Declaration of Competing Interest

The authors declare that they have no known competing financial interests or personal relationships that could have appeared to influence the work reported in this paper.

Appendix A. Supporting information

Supplementary data associated with this article can be found in the online version at doi:10.1016/j.jcou.2022.102069.

References

[1] W.J. Zhang, Y. Hu, L.B. Ma, G.Y. Zhu, Y.R. Wang, X.L. Xue, R.P. Chen, S.Y. Yang, Z. Jin, Progress and perspective of electrocatalytic CO_2 reduction for renewable carbonaceous fuels and chemicals, Adv. Sci. 5 (2018) 1700275.

[2] J. Resasco, A.T. Bell, Electrocatalytic CO_2 reduction to fuels: progress and opportunities, Trends Chem. 2 (2020) 825–836.

[3] J. Qiao, Y. Liu, F. Hong, J. Zhang, A review of catalysts for the electroreduction of carbon dioxide to produce low-carbon fuels, Chem. Soc. Rev. 43 (2014) 631–675.

[4] H. Jin, C. Guo, X. Liu, J. Liu, A. Vasileff, Y. Jiao, Y. Zheng, S.Z. Qiao, Emerging two-dimensional nanomaterials for electrocatalysis, Chem. Rev. 118 (2018) 6337–6408.

[5] T. Inoue, A. Fujishima, S. Konishi, K. Honda, Photoelectrocatalytic reduction of carbon dioxide in aqueous suspensions of semiconductor powders, Nature 277 (1979) 637–638.

[6] M. Halmann, Photoelectrochemical reduction of aqueous carbon dioxide on p-type gallium phosphide in liquid junction solar cells, Nature 275 (1978) 115–116.

[7] W. Li, Electrocatalytic reduction of CO_2 to small organic molecule fuels on metal catalysts, ACS Symp. Ser. 5 (2010) 55–76.

[8] T. He, L. Zhang, G. Kour, Electrochemical reduction of carbon dioxide on precise number of Fe atoms anchored graphdiyne, J. CO2 Util. 37 (2020) 272–277.

[9] D. Gao, R.M. Arán-Ais, H.S. Jeon, B.R. Cuenya, Rational catalyst and electrolyte design for CO_2 electroreduction towards multicarbon products, Nat. Catal. 2 (2019) 198–210.

[10] Z. Wang, J. Zhao, Q. Cai, CO_2 electroreduction performance of a single transition metal atom supported on porphyrin-like graphene: a computational study, Phys. Chem. Chem. Phys. 19 (2017) 23113–23121.

[11] J. Xie, X. Zhao, M. Wu, Q. Li, Y. Wang, J. Yao, Metal-free fluorine-doped carbon electrocatalyst for CO_2 reduction outcompeting hydrogen evolution, Angew. Chem. Int. Ed. 57 (2018) 9640–9644.

[12] T. Ma, Q. Fan, X. Li, J. Qiu, T. Wu, Z. Sun, Graphene-based materials for electrochemical CO_2 reduction, J. CO_2 Util. 30 (2019) 168–182.

[13] J. Zhang, T.S. Xu, D. Yuan, J.L. Tian, D.W. Ma, CO_2 electroreduction by transition metal embedded two-dimensional C_3N: A theoretical study, J. CO2 Util. 43 (2021) 101367.

[14] T. Cheng, H. Xiao, W.A. Goddard III, Reaction mechanisms for the electrochemical reduction of CO_2 to CO and formate on the Cu (100) surface at 298 K from quantum mechanics free energy calculations with explicit water, J. Am. Chem. Soc. 138 (2016) 13802–13805.

[15] K.P. Kuhl, E.R. Cave, D.N. Abram, T.F. Jaramillo, New insights into the electrochemical reduction of carbon dioxide on metallic copper surfaces, Energy Environ. Sci. 5 (2012) 7050–7059.

[16] B. Qiao, A. Wang, X. Yang, L.F. Allard, Z. Jiang, Y. Cui, J. Liu, J. Li, T. Zhang, Single-atom catalysis of CO oxidation using Pt_1/FeO_x, Nat. Chem. 3 (2011) 634–641.

[17] A.Q. Wang, J. Li, T. Zhang, Heterogeneous single-atom catalysis, Nat. Rev. Chem. 2 (2018) 65–81.

[18] T. Jin, D.M. Liang, M.S. Deng, S.H. Cai, X.S. Qi, Density functional theory studies of heteroatom-doped graphene-like GaN monolayers as electrocatalysts for oxygen evolution and reduction, ACS Appl. Nano Mater. 4 (2021) 7125–7133.

[19] S. Liu, H.B. Yang, S.F. Hung, J. Ding, W. Cai, L. Liu, J. Gao, X. Li, X. Ren, Z. Kuang, Y. Huang, T. Zhang, B. Liu, Elucidating the electrocatalytic CO_2 reduction reaction over a model single-atom nickel catalyst, Angew. Chem. Int. Ed. 59 (2020) 798–803.

[20] C. Ren, Q. Jiang, W. Lin, Y. Zhang, S. Huang, K. Ding, Density functional theory study of single-atom V, Nb, and Ta catalysts on graphene and carbon nitride for selective nitrogen reduction, ACS Appl. Nano Mater. 3 (2020) 5149–5159.

[21] X. Zhang, A. Chen, L. Chen, Z. Zhou, 2D materials bridging experiments and computations for electro/photocatalysis, Adv. Energy Mater. 12 (2021) 2003841.

[22] L.X. Chen, Z.W. Chen, M. Jiang, Z.L. Lu, C. Gao, G.M. Cai, C.V. Singh, Insights on the dual role of two-dimensional materials as catalysts and supports for energy and environmental catalysis, J. Mater. Chem. A 9 (2021), 2018-204223.

[23] X.Y. Chia, M. Pumera, Characteristics and performance of two-dimensional materials for electrocatalysis, Nat. Catal. 1 (2018) 909–921.

[24] S. Back, Y. Jung, TiC- and TiN-supported single-atom catalysts for dramatic improvements in CO_2 electrochemical reduction to CH_4, ACS Energy Lett. 2 (2017) 969–975.

[25] G. Xu, R. Wang, Y. Ding, Z. Lu, D. Ma, Z. Yang, First-principles study on the single Ir atom embedded graphdiyne: an efficient catalyst for CO oxidation, J. Phys. Chem. C 122 (2018) 23481–23492.

[26] C. Ao, B. Feng, S. Qian, L. Wang, W. Zhao, Y. Zhai, L. Zhang, Theoretical study of transition metals supported on g-C_3N_4 as electrochemical catalysts for CO_2 reduction to CH_3OH and CH_4, J. CO_2 Util. 36 (2020) 116–123.

[27] L. Fu, R. Wang, C.X. Zhao, J.R. Huo, C.Z. He, K.H. Kim, W. Zhang, Construction of Cr-embedded graphyne electrocatalyst for highly selective reduction of CO_2 to CH_4: A DFT study, Chem. Eng. J. 414 (2021), 128857.

[28] W.J. Wang, D. Li, T. Cui, Carbon and oxygen coordinating atoms adjust transition metal single-atom catalysts based on boron nitride monolayers for highly efficient CO_2 electroreduction, ACS Appl. Mater. Interfaces 13 (2021) 18934–18943.

[29] X. Wan, Z. Zhang, H. Niu, Y.H. Yin, C.G. Kuai, J. Wang, C. Shao, Y.Z. Guo, Machine-learning-accelerated catalytic activity predictions of transition metal phthalocyanine dual-metal-site catalysts for CO_2 reduction, J. Phys. Chem. Lett. 12 (2021) 6111–6118.

[30] M. Naguib, M. Kurtoglu, V. Presser, J. Lu, J. Niu, M. Heon, L. Hultman, Y. Gogotsi, M.W. Barsoum, Two-dimensional nanocrystals produced by exfoliation of Ti_3AlC_2, Adv. Mater. 23 (2011) 4248–4253.

[31] V. Kamysbayev, A.S. Filatov, H.C. Hu, X. Rui, F. Lagunas, D. Wang, R.F. Klie, D. V. Talapin, Covalent surface modifications and superconductivity of two-dimensional metal carbide MXenes, Science 369 (2020) 979–983.

[32] Y. Gogotsi, B. Anasori, The rise of mXenes, ACS Nano 13 (2019) 8491–8494.

[33] N. Li, X. Chen, W.J. Ong, D.R. MacFarlane, X. Zhao, A.K. Cheetham, C.H. Sun, Understanding of electrochemical mechanisms for CO_2 capture and conversion into hydrocarbon fuels in transition-metal carbides (MXenes), ACS Nano 11 (2017) 10825–10833.

[34] B.M. Jun, S. Kim, J. Heo, C.M. Park, N. Her, M. Jang, Y. Huang, J. Han, Y. Yoon, Review of MXenes as new nanomaterials for energy storage/delivery and selected environmental applications, Nano Res 12 (2018) 471–487.

[35] D. Zhao, Z. Chen, W. Yang, S. Liu, X. Zhang, Y. Yu, W.C. Cheong, L.R. Zheng, F. Q. Ren, G.B. Ying, X. Cao, D.S. Wang, Q. Peng, G.X. Wang, C. Chen, MXene (Ti_3C_2) Vacancy-confined single-atom catalyst for efficient functionalization of CO_2, J. Am. Chem. Soc. 141 (2019) 4086–4093.

[36] P. Urbankowski, B. Anasori, T. Makaryan, D. Er, S. Kota, P.L. Walsh, M. Zhao, V. B. Shenoy, M.W. Barsoum, Y. Gogotsi, Synthesis of two-dimensional titanium nitride Ti$_4$N$_3$ (MXene), Nanoscale 8 (2016) 11385–11391.

[37] X.H. Zha, K. Luo, Q. Li, Q. Huang, J. He, X. Wen, S. Du, Role of the surface effect on the structural, electronic and mechanical properties of the carbide MXenes, EPL 111 (2015) 26007.

[38] Y. Xie, M. Naguib, V.N. Mochalin, M.W. Barsoum, Y. Gogotsi, X. Yu, K.W. Nam, X. Q. Yang, A.I. Kolesnikov, P.R. Kent, Role of surface structure on Li-ion energy storage capacity of two-dimensional transition-metal carbide, J. Am. Chem. Soc. 136 (2014) 6385–6394.

[39] T. Schultz, N.C. Frey, K. Hantanasirisakul, S. Park, S.J. May, V.B. Shenoy, Y. Gogotsi, N. Koch, Surface termination dependent work function and electronic properties of Ti$_3$C$_2$T$_x$ MXene, Chem. Mater. 31 (2019) 6590–6597.

[40] O. Mashtalir, M.R. Lukatskaya, M.Q. Zhao, M.W. Barsoum, Y. Gogotsi, Amine-assisted delamination of Nb$_2$C MXene for Li-ion energy storage devices, Adv. Mater. 27 (2015) 3501–3506.

[41] T. Su, R. Peng, Z.D. Hood, M. Naguib, I.N. Ivanov, J.K. Keum, Z. Qin, Z. Guo, Z. Wu, One-step synthesis of Nb$_2$O$_5$/C/Nb$_2$C (MXene) composites and their use as photocatalysts for hydrogen evolution, ChemSusChem 11 (2018) 688–699.

[42] D. Kan, D. Wang, X. Zhang, R. Lian, J. Xu, G. Chen, Y. Wei, Rational design of bifunctional ORR/OER catalysts based on Pt/Pd-doped Nb$_2$CT$_2$ MXene by first-principles calculations, J. Mater. Chem. A 8 (2020) 3097–3108.

[43] G. Kresse, D. Joubert, From ultrasoft pseudopotentials to the projector augmented-wave method, Phys. Rev. B 59 (1999) 1758.

[44] G. Kresse, J. Furthmüller, Efficiency of ab-initio total energy calculations for metals and semiconductors using a plane-wave basis set, Comput. Mater. Sci. 6 (1996) 15–50.

[45] J.P. Perdew, K. Burke, M. Ernzerhof, Generalized gradient approximation made simple, Phys. Rev. Lett. 77 (1996) 3865–3868.

[46] J.P. Perdew, M. Ernzerhof, K. Burke, Rationale for mixing exact exchange with density functional approximations, J. Chem. Phys. 105 (1996) 9982–9985.

[47] S. Grimme, J. Antony, S. Ehrlich, H. Krieg, A consistent and accurate ab initio parametrization of density functional dispersion correction (DFT-D) for the 94 elements H-Pu, J. Chem. Phys. 132 (2010) 154104–154123.

[48] K. Mathew, R. Sundararaman, K.L. Weaver, T.A. Arias, R.G. Hennig, Implicit solvation model for density-functional study of nanocrystal surfaces and reaction pathways, J. Chem. Phys. 140 (2014) 084106–084114.

[49] G. Kresse, J. Hafner, Ab initio molecular dynamics for liquid metals, Phys. Rev. B 47 (1993) 558.

[50] S. Baroni, S. de Gironcoli, A. dal Corso, P. Giannozzi, Phonons and related crystal properties from density-functional perturbation theory, Rev. Mod. Phys. 73 (2001) 515.

[51] D. Sheppard, R. Terrell, G. Henkelman, Optimization methods for finding minimum energy paths, J. Chem. Phys. 128 (2008), 134106.

[52] G. Henkelman, A. Arnaldsson, H. Jónsson, A fast and robust algorithm for Bader decomposition of charge density, Comp. Mater. Sci. 36 (3) (2006) 354–360.

[53] J.K. Nørskov, J. Rossmeisl, A. Logadottir, L. Lindqvist, J.R. Kitchin, T. Bligaard, H. Jonsson, Origin of the overpotential for oxygen reduction at a fuel-cell cathode, J. Phys. Chem. B 108 (2004) 17886–17892.

[54] Y. Wang, W. Tian, H. Zhang, Y. Wang, Nb2N monolayer as a promising anode material for Li/Na/K/Ca-ion batteries: a DFT calculation, Phys. Chem. Chem. Phys. 23 (2021) 12288–12295.

[55] S.S. Zheng, C.J. Zuo, X.H. Liang, S.N. Li, F. Pan, Valence state of transition metal center as an activity descriptor for CO$_2$ reduction on single atom catalysts, J. Energy Chem. 56 (2021) 444–448.

[56] F.F. Li, H.Q. Ai, C.M. Shi, K.H. Lo, H. Pan, Single transition metal atom catalysts on Ti$_2$CN$_2$ for efficient CO$_2$ reduction reaction, Int. J. Hydrog. Energy 46 (2021) 12886–12896.

[57] Y. Hori, H. Wakebe, T. Tsukamoto, O. Koga, Electrocatalytic process of CO selectivity in electrochemical reduction of CO$_2$ at metal electrodes in aqueous media, Electrochim. Acta 39 (1994) 1833–1839.

[58] C. Guo, T. Zhang, X. Deng, X. Liang, W. Guo, X. Lu, C.M.L. Wu, Electrochemical CO$_2$ reduction to C1 products on single nickel/cobalt/iron-doped graphitic carbon nitride: a DFT study, ChemSusChem 12 (2019) 5126–5132.

[59] S. Lu, H.L. Huynh, F.L. Lou, M. Guo, Z.X. Yu, Electrochemical reduction of CO$_2$ to CH$_4$ over transition metal atom embedded antimonene: first-principles study, J. CO$_2$ Util. 51 (2021) 101645.

[60] G. Kour, X. Mao, A.J. Du, Computational screening of transition metal–phthalocyanines for the electrochemical reduction of carbon dioxide, J. Phys. Chem. C 124 (2020) 7708–7715.

[61] J.K. Nørskov, T. Bligaard, A. Logadottir, J.R. Kitchin, J.G. Chen, S. Pandelov, U. Stimming, Trends in the exchange current for hydrogen evolution, J. Electrochem. Soc. 152 (2005) J23–J26.

[62] L. Li, X. Wang, H. Guo, G. Yao, L. Chen, Theoretical screening of single transition metal atoms embedded in MXene defects as superior electrocatalyst of nitrogen reduction reaction, Small Methods 3 (2019) 1900337.